THE JOURNAL OF
PHYSICAL CHEMISTRY C

ARTICLE

pubs.acs.org/JPCC

Can We Control the Thickness of Ultrathin Silica Layers by Hyperthermal Silicon Oxidation at Room Temperature?

U. Khalilov,*[†] E. C. Neyts,[†] G. Pourtois,[†,‡] and Adri C. T. van Duin[§]

[†]Department of Chemistry, PLASMANT Research Group, University of Antwerp, Universiteitsplein 1, B-2610 Wilrijk-Antwerp, Belgium

[‡]IMEC, Kapeldreef 75, B-3001 Leuven, Belgium

[§]Department of Mechanical and Nuclear Engineering, Penn State University, University Park, Pennsylvania 16801, United States

S *Supporting Information*

ABSTRACT: Using reactive molecular dynamics simulations by means of the ReaxFF potential, we studied the growth mechanism of ultrathin silica (SiO_2) layers during hyperthermal oxidation at room temperature. Oxidation of Si(100){2 × 1} surfaces by both atomic and molecular oxygen was investigated in the energy range 1−5 eV. The oxidation mechanism, which differs from thermal oxidation, is discussed. In the case of oxidation by molecular O_2, silica is quickly formed and the thickness of the formed layers remains limited compared to oxidation by atomic oxygen. The Si/SiO_2 interfaces are analyzed in terms of partial charges and angle distributions. The obtained structures of the ultrathin SiO_2 films are amorphous, including some intrinsic defects. This study is important for the fabrication of silica-based devices in the micro- and nanoelectronics industry, and more specifically for the fabrication of metal oxide semiconductor devices.

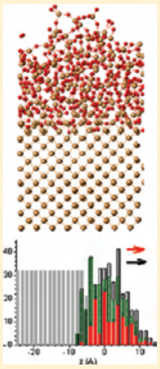

1. INTRODUCTION

Silicon dioxide (SiO_2) films can nowadays successfully be grown on crystal silicon, with a thickness of a few monolayers.[1,2] This is important for the fabrication of microelectronics and photovoltaic devices (e.g., metal oxide semiconductor field-effect transistors (MOSFETs), solar cells, optical fibers, etc.).[1−7] In such thin films, a significant portion of the film is occupied by the transition layer at the Si/SiO_2 interface, degrading the dielectric properties, the light absorption efficiency, and hence the performances of the devices. Being able to control atomically the interface is however a challenging task for near future nanoelectronics.[1,2] Therefore, understanding the growth process at the atomic scale (i.e., oxidation kinetics and dynamics, transport phenomena during oxidation, etc.) of ultrathin silicon dioxide is of prime importance.[2,8]

In fact, the most generally adopted model for silicon oxidation is the Deal−Grove model.[9] In this model, it is assumed that an oxide species first enters the SiO_2 layer, then diffuses through the disordered oxide toward the Si/SiO_2 interface, and finally reacts at the Si substrate, where the new oxide grows. Unfortunately, this model does not accurately describe the kinetics of the silicon oxidation for thin layers (<100 Å),[10−12] although certain key aspects of the model are still accurate for films with thickness above 40 Å at high temperature (>1000 K),[10,11] including oxygen diffusion in the Si/SiO_2 interface and oxide formation at the interface. However, the mechanism clearly fails when describing the oxidation kinetics of ultrathin films (∼20 Å) at room temperature.[8,12] Furthermore, several extensions of the model have been proposed to describe the growth rate enhancement in thin oxide regime, for example, the Massoud−Plummer−Irene extension,[13] reporting data for the oxidation rate for layers between about 20 Å and 500 Å in detail. However, there is little or no experimental data extending continuously from 20 Å downward.[5]

The analysis of physical properties[14−19] of the SiO_2/Si(100) system, as well as the behavior of the Si/SiO_2 interface during oxidation by hyperthermal oxygen species at room temperature[4,20−22] has already received a lot of attention. Oxidation kinetics and growth mechanisms at room temperature were properly analyzed in the thermal oxidation regime. Cerofolini et al.[23,24] presented a model for oxidation kinetics in air at room temperature of single crystalline and hydrogen terminated (100) silicon. They properly elucidated the growth mechanism, that is, formation and growth behavior of the substoichiometric and stoichiometric oxides. The kinetics were described by the Elovich equation in the long-time limit. While the equation describes the linear-saturation behavior of oxygen coverage on Si surface well, the kinetic model fails in two situations for describing the hyperthermal oxidation: (a) no solution of the equation for the formation of substoichiometric oxides exists for the case $\theta(0) = 0$; (b) there are no suitable parameters for describing the direct oxidation, that is, energetic oxygen species directly oxidizing the

Received: August 26, 2011
Revised: October 25, 2011
Published: November 15, 2011

Si subsurface layers. Indeed, the growth mechanism of silicon dioxide in the initial state of hyperthermal oxidation has not yet been properly analyzed, and investigations at the atomic scale are required. Therefore, we carried out reactive molecular dynamics (MD) calculations for clarifying the formation and growth behavior of SiO_2 on a Si(100){2 × 1} reconstructed surface at room temperature during oxidation by oxygen species (O, O_2) with hyperthermal energies (1−5 eV), and the resulting silica thickness.

2. COMPUTATIONAL DETAILS

2.1. Interatomic Potential. In a MD simulation, the path of the atoms is followed through space and time by integrating the equations of motion. In this work, the forces on the atoms are derived from the Reactive Force Field (ReaxFF) potential.[25]

The ReaxFF potential uses the bond order/bond distance relationship formally introduced by Abell.[26] The total system energy is the sum of several partial energy terms; these include energies related to lone pairs, undercoordination, overcoordination, valence and torsion angles, conjugation, hydrogen bonding, as well as van der Waals and Coulomb interactions. Charge distributions are calculated based on geometry and connectivity using the electronegativity equalization method (EEM).[27] A detailed description of the force field can be found elsewhere.[28−30] Currently, the ReaxFF potential is successfully being applied to a few tens of elements and their compounds, including hydrocarbons,[25] silicon/silicon oxide,[31−33] metals, metal oxides,[34] and metal hydrides.[35]

2.2. Simulation Method. For the simulation, a Si(100)-{2 × 1} reconstructed surface is chosen, with dimensions 21.7 Å × 21.7 Å × 27.1 Å. Periodic boundary conditions are applied to the {*xy*} plane, to mimic a laterally infinite surface. Prior to the impact simulations, the box is equilibrated at 300 K using the Berendsen heat bath.[36] The obtained structure is subsequently relaxed in the microcanonical ensemble for 10 ps.

Oxygen impacts are performed as follows. The incident particle (oxygen atom or oxygen molecule) is positioned at a *z* position of 10 Å above the uppermost Si atom of the crystal. The {*x*, *y*} coordinates of the incident particles are chosen randomly. In the case of molecular oxygen, the O_2 molecule is rotated randomly prior to impact. The impinging particle is directed normal to the surface, corresponding to laser detonation experiments.[37,38] Every impact is followed for 3 ps. Three series of simulations were carried out for kinetic energies of the impinging oxygen species (O, O_2) of 1, 3, and 5 eV.

3. RESULTS AND DISCUSSION

3.1. Growth Process. *3.1.1. Two-Stage Hyperthermal Oxidation.* A general evolution of the growth process is presented in Figure 1. Figure 1a shows the evolution of the oxygen content of the Si lattice as a function of O fluence in monolayers (ML) for both atomic and molecular impact cases with initial kinetic energies of 1, 3, and 5 eV. In our calculations one ML corresponds to 32 atoms. It can be seen in the figure that the oxidation process can be divided into two stages: (I) the initial fast oxidation stage and (II) the subsequent slow oxidation stage. This corresponds to previous experimental studies.[11,39] In the first stage, the oxygen content rapidly increases due to the high adsorption probability of the oxygen species on the pure silicon surface. In this stage, the silicon surface and subsurface layers are directly oxidized by hyperthermal oxygen species.[4,19,37] Consequently, the oxygen sticking probability is in this stage not a function of the oxygen fluence (Figure 1b), and the oxygen content grows linearly. The duration of the first stage strongly depends on incident energy and type of oxygen species. The results indicate that the first stage continues for 2.6, 5.0, and 6.2 ML of oxygen fluence in the atomic case with 1, 3, and 5 eV, respectively. In the molecular case, the duration of stage I is shorter due to the lower adsorption probability, and it lasts for about 1.6, 2.4, and 2.6 ML, respectively, for initial kinetic energies of 1, 3, and 5 eV.

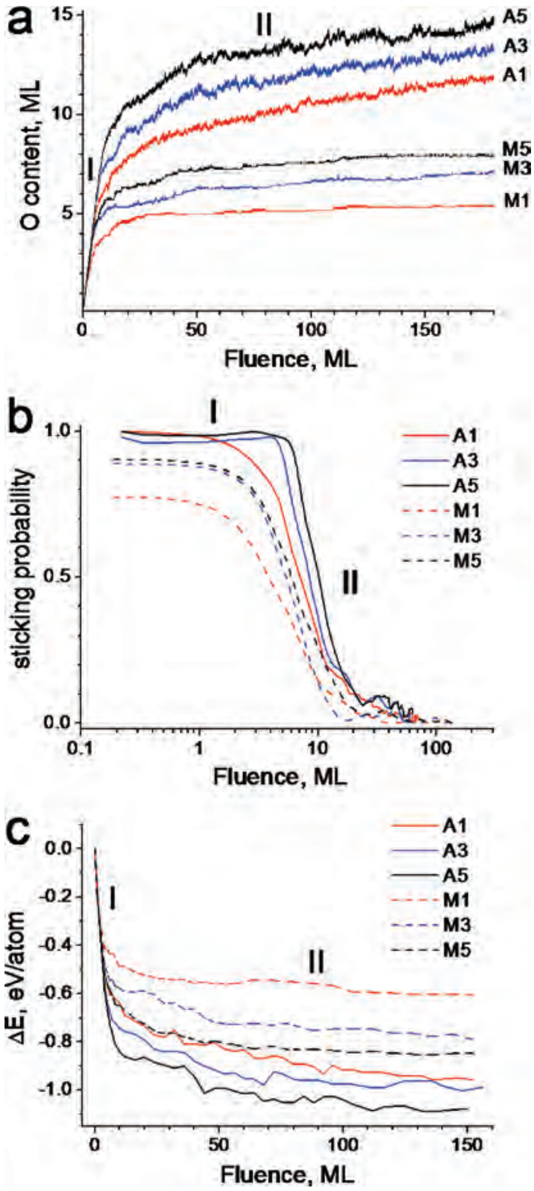

Figure 1. Oxidation stages (I and II) during hyperthermal oxidation (1−5 eV) on the {2 × 1} reconstructed Si(100) surface at room temperature: (a) oxygen coverage on the silicon surface, (b) adsorption behavior of incident oxygen species, and (c) variation of total energy of the SiO_2/Si system as a function of fluence, for both atomic (A1−1 eV, A3−3 eV, A5−5 eV) and molecular (M1−1 eV, M3−3 eV, M5−5 eV) oxygen beams.

In the beginning of the second stage, the sticking probability of the incident oxygen species decreases rapidly due to the presence

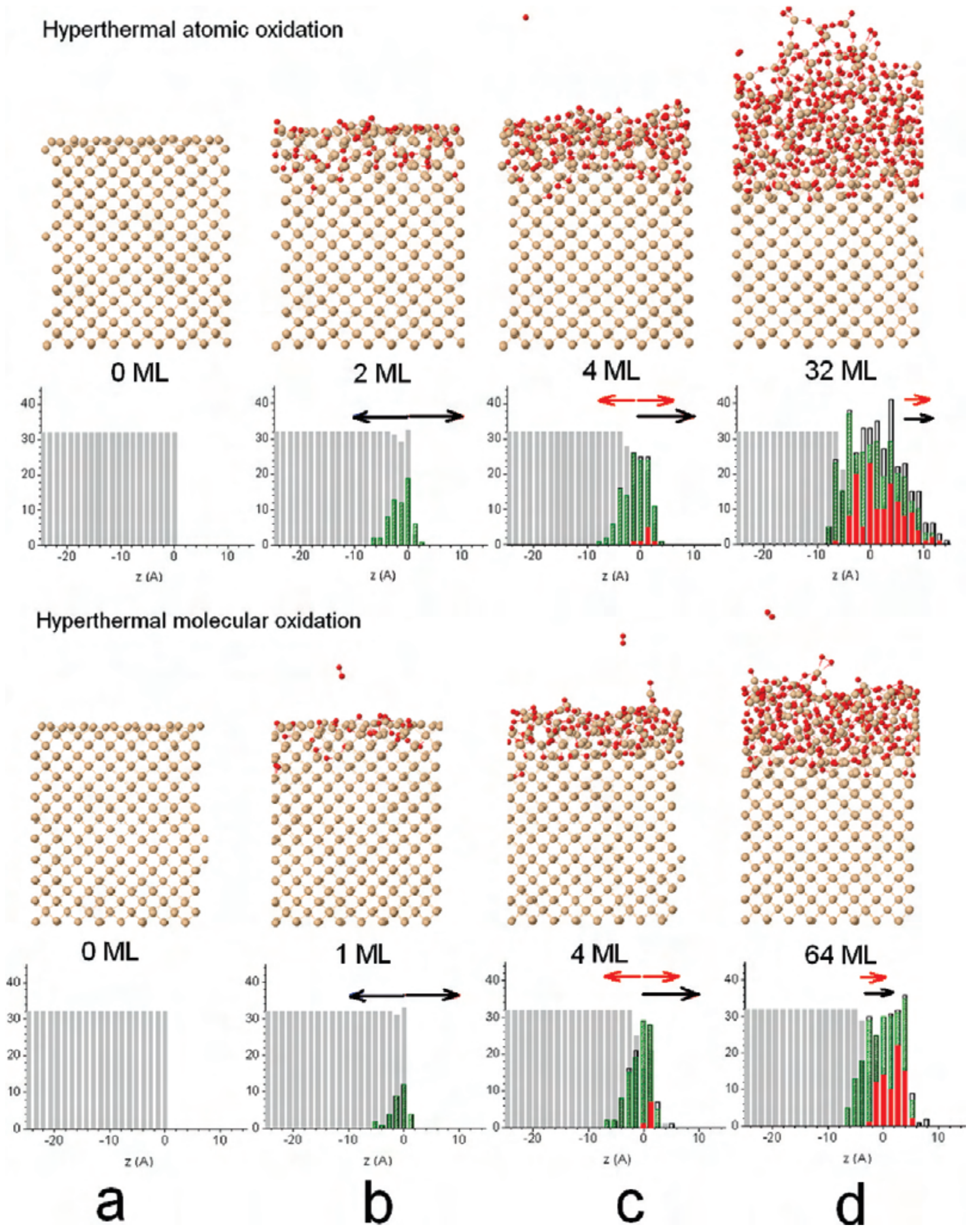

Figure 2. Growth behavior of ultrathin silica layers induced by 5 eV atomic and molecular oxygen at room temperature. The occurrence of pure Si, SiO_x, and SiO_2 is indicated in the histograms by light gray bars, green bars, and red bars, respectively. Black and red arrows indicate the growth direction of the oxidized and silica layers, respectively.

of the previously adsorbed oxygen atoms, which appear on the topmost layer of the newly formed silica layer. As a result, most of the new impacting oxygen atoms do not link to the surface atoms during this stage. This leads to a gradual saturation of the oxygen content. In the molecular impact case, the saturation occurs much faster than in the atomic case.

While the oxygenated silicon thickness quickly increases in the first stage, the main effect of the second stage is structural change. Figure 1c presents the energy gain of the SiO_2/Si interface due to oxidation. In the first stage, the energy curve drops (i.e., becomes more negative) much more quickly than in the second stage. The energy plot indicates that oxygenated silicon is energetically more stable than pure silicon. As shown in Figure 1c, the total energy of the oxygenated silicon bulk strongly depends on energy and type of incident oxygen species, that is, the system appears to become more stable upon atomic impacts than upon molecular impacts, and also with increasing energy of the impacting species. Indeed, the energy gain depends on the extent of the Si−O bonding, which is analyzed below.

3.1.2. Growth Mechanism of Ultrathin SiO_2 Layers during Hyperthermal Oxidation.

In Figure 2, the SiO_2 growth process on a {2 × 1} reconstructed Si(100) surface by both oxygen atoms and molecules with an incident energy of 5 eV is presented. The oxidation progress is shown by molecular structure representations and suboxide histograms. Here, gray, green, and red bars describe the density distribution per depth of pure Si, oxygenated Si (i.e., SiO_x) species and ultrathin silica (i.e., SiO_2) layers, respectively. $z = 0.0$ Å corresponds to the topmost layer of the original pristine Si lattice.

Our calculations are based on the mass center position of Si layer planes[40] and show that the average thickness of each layer is equal to 1.296 Å, corresponding to the thickness of one-half oxide layer (one oxide layer thickness is 2.6 Å[4]).

We can distinguish two steps in the growth mechanism of silica layers at room temperature. In the first step, the oxidized layers grow simultaneously inward and outward, normal to the surface (see Figure 2b in both the atomic and molecular impact case; the black arrows indicate the growth direction of oxidized layers). However, due to the associated activation energy barrier of the Si subsurface layers, which is on the order of 1 eV,[41,42] the inward growth is interrupted quickly, and atoms cannot penetrate in the crystal any further. This indicates the end of the initial growth step. Consequently, during the entire oxidation process, the penetrated oxygen atoms can move only up to the limit depth. The limit of the oxidized depth is equal to the maximum penetration depth of the oxygen atoms, and it determines the maximum number of silicon atoms, which may contribute to the formation of the oxygenated silicon layers. The results show that the limit depth is nearly constant during the second oxidation stage and it depends on both kinetic energy and type of incident oxygen species. The maximum penetration depth was found to be 8, 9, and 10 Å during the atomic oxidation with kinetic energies 1, 3, and 5 eV, respectively. In the molecular oxidation case, the limit depths were slightly less than in the atomic case, and the values were equal to 4, 6.9, and 7 Å for kinetic energies of 1, 3, and 5 eV, respectively. The limit depths are very close to the values of our previous calculations.[43]

When the second growth step starts, an "incipient" silica layer appears (Figure 2c in both the atomic and molecular impact case). The results demonstrate that silica also grows in two directions during the second step (the red arrows indicate the growth direction of silica in Figure 2c,d). Inward growth of silica continues up to the interface area, which is located between silica (SiO_2) and crystalline Si. When the oxygen content is completely saturated, only the outward silica growth continues (see Figure 2d). Indeed, in the molecular case, the maximum silica thickness is nearly constant during the second oxidation stage. Furthermore, in this case, silica formation is almost completed at the beginning of the second stage, and the silica layer is thinner due to fast saturation of the oxygen content and the low limit depth of penetrated oxygen atoms. The maximum thickness is reached when also the outward growth of the silica stops (not shown in Figure 2).

3.1.3. Evolution of Si Suboxide Components in the Initial Oxidation Stage. As was mentioned in Section 3.1.1, a direct insertion of oxygen atoms into the Si subsurface layers is found during the initial stage, for hyperthermal oxidation at room temperature, which has not been observed in thermal oxidation. On the other hand, in the hyperthermal energy regime, incident atoms can surmount the energy barriers of the first or even second subsurface layers,[43] which are estimated to be about 1.0 and 2.4 eV, respectively.[41] Such oxidation behavior was also studied by ellipsometry and synchrotron radiation photoemission spectroscopy.[4,19,37] The temporal evolution of the formation and growth of the oxygenated silicon in the initial oxidation stage can easily be understood by observing the variation of the silicon suboxide components. Generally, the components Si^{1+}, Si^{2+}, Si^{3+}, and Si^{4+} are supposed to arise from interfacial silicon atoms, which bind to one, two, three, and four nearest-neighbor oxygen atoms, respectively, that is, this corresponds to Si_2O, SiO, Si_2O_3, and SiO_2, respectively. Figure 3a shows the variation of the relative concentrations of Si suboxide species in order to elucidate the oxidation behavior in the initial stage. In this stage, an adsorbed oxygen atom can bind to surface atoms in different configurations. Previous studies[41,44,45] demonstrated back-bond (B), dimer-bridge (D), on-dimer (D1), and on-top (T) structures on the initial Si (100) structure (see pictures in Figure 3b). It was argued that the B or D bonds are energetically most favorable.[41,44−46]

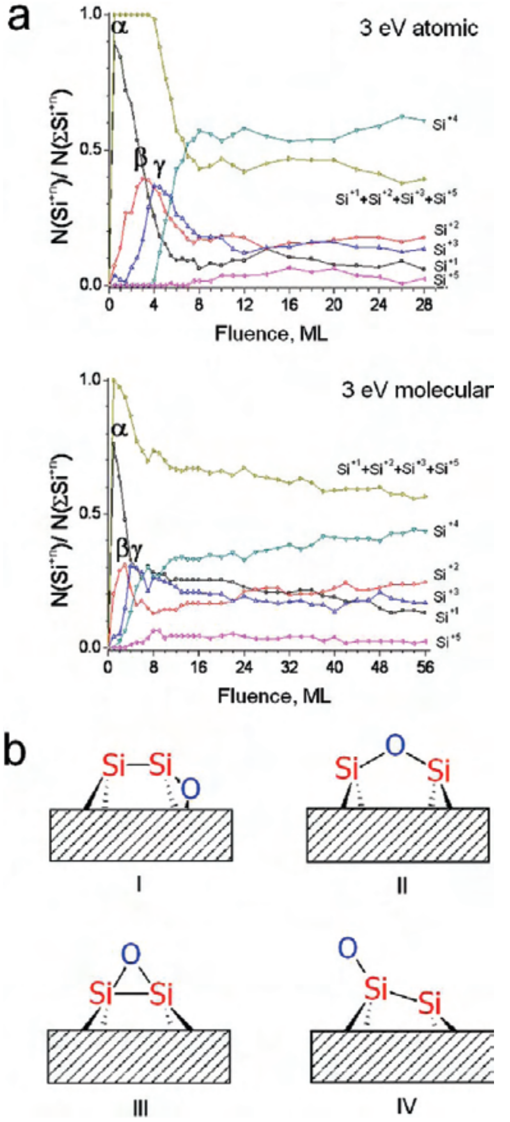

Figure 3. (a) Relative numbers of silicon suboxide components as a function of atomic and molecular oxygen fluence. (b) Possible bond configurations of an oxygen atom with a Si(100){2 × 1} surface in the initial silicon oxidation: (I) back-bond (B), (II) dimer-bridge (D), (III) on-dimer (D1), and (IV) on-top (T) structures.

In our case, each of these Si−O bond configurations, except the D structure, are found during the initial oxidation stage. As can be seen in Figure 3a, the Si^{1+} peak (α) initially dominates. Indeed, in the earliest stage, the adsorbed oxygen atoms bind according to one of the bond configurations as shown in Figure 3b. The D configuration is found as soon as the first subsurface layer becomes oxidized. The Si^{2+} peak (β) indicates the appearance of two bonds, that is, BB, BD, BT, or BD1, of which BB and BD1 dominate. The appearance of mainly BBD, BBD1, and BDT bonds is represented by the Si^{3+} peak (γ). In Figure 3a, it is shown both in the atomic and molecular oxidation case, that Si^{1+}, Si^{2+}, and Si^{3+} suboxide species consecutively dominate in the initial oxidation stage. All of these three Si suboxide species are found in the first few tens of impacts. Indeed, incident oxygen can penetrate deeper than the Si topmost surface and directly oxidizes the Si subsurface layers, that is, the uppermost (no barrier energy[41]) and first subsurface layers (barrier energy about 1 eV[41]). When the silica layer appears, the Si^{4+} curve increases continuously, and the other suboxide components significantly decrease, as is clear from Figure 3a. Note that the yellow curve in both the atomic and molecular case denotes the sum of Si^{1+}, Si^{2+}, Si^{3+}, and Si^{5+}, whereas the blue curve gives the Si^{4+} contribution; the sum of these two curves is equal to 1.

This behavior allows us to assess when the SiO_2 growth starts, that is, after about 4 ML in the atomic case, and after about 2 ML in the molecular case. Note that our calculations also some five-fold suboxide species are detected in the silica bulk during the oxidation process, although in very low concentration, which is due to residual uncorrected overbinding in the potential.

3.1.4. Charge Distribution of the Si(100)/SiO_x/SiO_2 System during Oxidation. Calculation of the charge distribution facilitates to identify two regions of the oxidized silicon: transition (SiO_x) and silica (SiO_2). In Figure 4, partial charge distributions of Si and O in the SiO_2/SiO_x/Si(100) structure are shown for oxidation by atomic and molecular oxygen, for an energy of 3 eV. In the transition region (colored dark gray), the partial charges of Si and O atoms range approximately from 0 to $+1.2e$ and from $-0.9e$ to $-0.6e$, respectively. On the other hand, the average partial charges are about $+1.2e$ and $-0.6e$ in the SiO_2 region (colored light gray) for Si and O atoms, respectively. Indeed, analysis of the obtained oxygenated silicon bulk during the oxidation process by the partial charge distribution clearly shows that the bulk is split up in two regions: a transition layer and silicon dioxide (or pure silica), which is consistent with experimental and theoretical studies.[11,16,47] The charges of the oxygen atoms are distributed in the range between $-0.3e$ and $-0.6e$ in the case of atomic oxidation because of peroxyl and three-fold oxygen bond configurations in the silica region (see below). Furthermore, also some Si−Si bonds (i.e., oxygen vacancies)[48] are found in the SiO_2 region in the molecular oxidation case. Previous DFT calculations[47] suggested that such a distribution in the silica region is induced by oxygen-deficient defects. Moreover, due to intrinsic defects (i.e., an incorrect coordination of a Si or O atom, or a Si−Si or an O−O bond), the total charge of the oxygenated silicon area is locally not zero. We believe that some O−O peroxyl bridge and three-fold oxygen bond configurations[17,48] in SiO_2 disorder the charge distribution of the oxygen atoms. In addition, oxygen atoms, which are distributed in the top oxide layer, strongly affect the incident oxygen species during oxidation. This effect may accelerate the saturation of the oxygen content in the molecular case. Finally, note that the calculated charges are determined from the EEM method, fitted to Mulliken charges. As Mulliken charges are heavily dependent on the basis set used, the exact values should not be taken too literally. Nevertheless, the obtained values are in reasonable agreement with experimental values for quartz and coesite.[49]

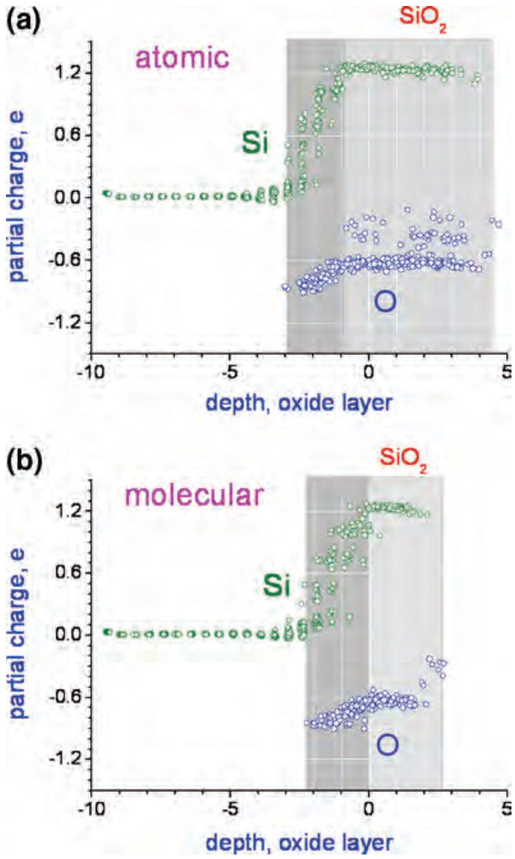

Figure 4. Charge distributions of Si and O in the Si(100)/SiO_x/SiO_2 system, for (a) atomic and (b) molecular oxidation, for a kinetic energy of 3 eV. The oxidized Si (i.e., SiO_x) transition layer and the silica (SiO_2) bulk can clearly be identified by the dark gray and lighter gray regions, respectively.

3.1.5. Variation of the Thickness of the Interface (or Transition Layer) between Pure Si and SiO_2 during Oxidation. In Section 3.1.4, the partial charge distribution also indicates that all Si suboxide components are found in the oxygenated silicon region. The silicon suboxide species allow analysis of the transition area as well. In the transition or nonstoichiometric oxide region, located between the crystalline silicon and the silicon dioxide (silica) layer, all three Si suboxide species (Si^{1+}, Si^{2+}, and Si^{3+}) are found. Our calculations predict that the oxygen density is somewhat higher in the transition region than in the pure silica bulk, as is also experimentally found[11] through the analysis of the oxygenated silicon bulk as grown by thermal oxidation. Both the temporal variation of the silicon suboxide components and the partial charge distribution predict that the transition area is thinner than the SiO_2 bulk. In Figure 5, the variation in thickness of the transition layer, also called interface, during hyperthermal oxidation by oxygen species is shown. For both atomic and molecular oxidation, the thickness of the transition area increases with increasing thickness of the oxygenated silica during the initial oxidation stage. In the second stage, the thicknesses of the transition area slightly decrease again and become about 5 Å. This value corresponds to the lower limit of several experimental measurements,[10,11,14] in which the thickness of the transition region ranges from 5 to 50 Å. Moreover, this value seems to be rather independent from the energy and type (atomic/molecular) of the impacting species.

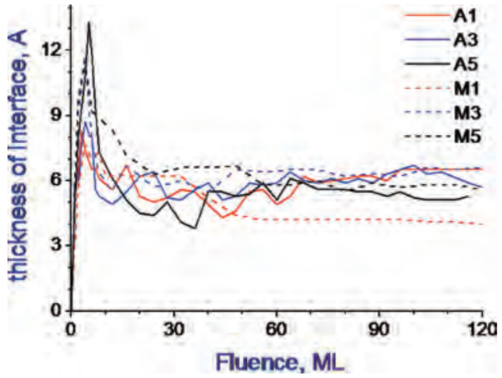

Figure 5. Variation of the interface thickness during hyperthermal oxidation, as a function of the oxygen fluence, for both atomic and molecular impacts of 1, 3, and 5 eV.

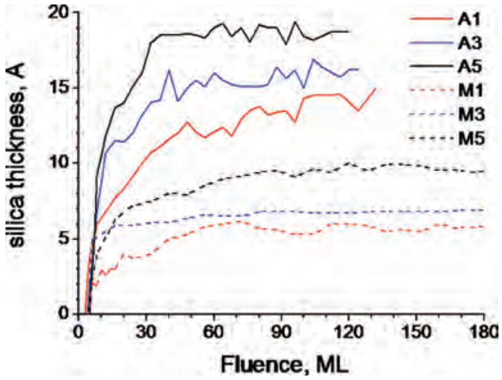

Figure 6. Variation of the SiO_2 thickness as a function of the oxygen fluence, for both atomic and molecular impacts of 1, 3, and 5 eV.

3.1.6. Variation of the SiO_2 Thickness during Oxidation. Figure 6 shows the temporal evolution (or evolution as a function of oxygen fluence) of the thickness of the pure silica layer during hyperthermal oxidation. As mentioned above, the silica appears when a few ML of oxygen is incorporated during the initial oxidation stage. In the initial oxidation stage, the silica layer grows rapidly. Our results predict that the increase in the silica thickness consists of two stages: a linear and a nonlinear stage.

A linear increase in the silica thickness is observed during the initial oxidation stage. This linearity was also found by using ellipsometry and synchrotron radiation photoemission spectroscopy,[37] in which the limits of the linear growth for 1.8, 2.7, 3.8, and 5.0 eV were 3.0, 6.2, 6.2, and 7.0 Å, respectively. Our calculations show that the limits of linear growth during hyperthermal oxidation with oxygen atoms for incident energies of 1, 3, and 5 eV are about 2.0, 6.0, and 9.0 Å, respectively, which differs only slightly from the experimental result. This linearity was also observed in the molecular case, although only during a relatively shorter time.

In the molecular oxidation case, the thickness quickly becomes constant at the start of the second oxidation stage due to the next-to-complete saturation of the oxygen content. However, the silica thickness slightly oscillates around an average thickness value due to the consecutive hyperthermal oxygen impacts and increasing stress of the Si(100)/SiO_2 system, due to which, the topmost silica layer is significantly damaged after each atomic impact.

Analysis of the fluctuations induced by molecular oxygen with an energy of 3 eV shows that the average value of the thickness is about 6.3 Å. This is close to the experimental value of 6 Å,[4] which was obtained by using supersonic O_2 molecular beams at room temperature. Our results predict that, in the molecular oxidation cases with energies of 1 and 5 eV, the average values of the silica thickness are about 5 and 9 Å, respectively.

In the atomic case, the minimum thickness of the final silica configuration was not less than 5.5 oxide layers (~14 Å) for the 1 eV impacts, and it increases with higher impact energy, to about 15 Å at 3 eV and 18.5 Å at 5 eV. This value is also close to the experimental value of 17.5 Å, which was obtained at 493 K by oxygen atoms with kinetic energy of 4.6 eV.[39] However, this oxidation was performed on a H-terminated Si(001) surface using a relatively low oxygen fluence. The thickness obtained at 5 eV is also in close agreement with other experimental results.[19]

Analysis of the thickness variations assumes that the change in silica thickness as a function of incident energy is smaller for the molecular oxidation than for the atomic one due to the immediate breakup upon collision of the molecules. Indeed, as the molecules are given the same initial kinetic energy as the atoms, the individual atoms obtained after dissociation have less momentum and hence a lower velocity. Therefore, oxygen molecules do not penetrate as deep in the surface as the oxygen atoms. However, hyperthermal O_2 molecules are found to be more effectively than oxygen atom for controlling the ultrathin oxide thickness at room temperature.

3.2. Analysis of the Obtained Films.

3.2.1. Roughness of the SiO_2/Si Interface (Transition Region). The roughness of the SiO_2/Si interface is a crucial parameter for ultrathin films. Indeed, careful analysis of the interface roughness at the atomic scale is quite important for MOSFET technology, for example. Therefore, we analyzed the interface between ultrathin SiO_2 and crystalline Si. As mentioned in Section 3.1.5, the thickness of all interfaces (or transition layers, which consist of Si^{1+}, Si^{2+}, and Si^{3+} suboxide components) is almost constant and is limited to about 5 Å during the second oxidation stage. In Figure 7, six interfaces, obtained after 150 ML of oxygen fluence during both atomic and molecular oxidation with 1, 3, and 5 eV, are shown. As can be seen, the interface with the crystalline Si is very sharp. Clearly, the interface is sharper in the structures obtained by 1 eV atomic and molecular oxidation than other structures. The root-mean-square surface roughness of the interface is low. Moreover, analysis of the surface indicates that some small protrusions exist in the ultrathin nonstoichiometric oxide region, which is presented also in the Irene's interface model for the thermal oxidation case.[14] In a forthcoming paper, a more detailed analysis, including stress calculations, will be presented.

3.2.2. Analysis by Means of Mass and Charge Distribution. As was mentioned above, the oxidized silicon layer can be divided into two parts: a near-interface region ("transition layer") and a pure silica region. Furthermore, the pure silica region can also be divided in bulk and surface parts.[11] In Figure 8, the oxygenated silicon layer is schematically represented by both the mass and charge distributions. In the mass distribution graph, the resolution of the analyzed layer thickness is 2.592 Å, which corresponds to the thickness of one oxide layer. The oxygenated silicon layer is divided into three parts by means of the obtained mass and partial charge distributions, that is, interface, silica bulk, and silica surface (indicated by II, III, and IV, respectively, in Figure 8; region I is the pure Si region). Gusev et al.[11] clearly showed the presence of these three parts in their relatively thicker oxide films

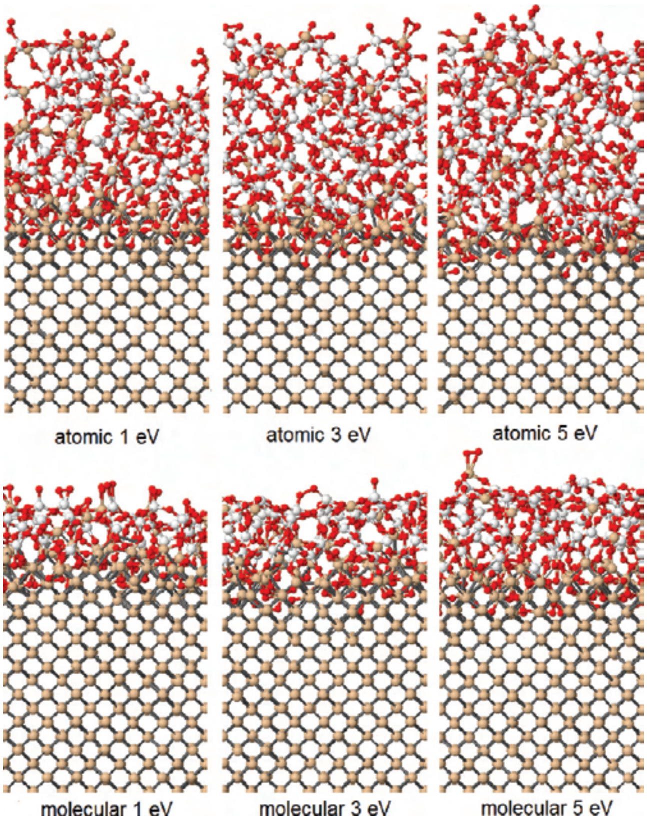

Figure 7. SiO_2/Si interfaces (dark gray regions) obtained by both atomic and molecular oxidation with 1, 3, and 5 eV. White and gray silicon atoms indicate ultrathin SiO_2 and crystalline Si, respectively.

(~ 50 Å), as obtained by thermal oxidation at 1020−1170 K. They also explained that these regions overlap in ultrathin oxide films (~ 20 Å) during the oxidation process. Such an overlapping was also found in our obtained oxide films. The mass distribution shows that relatively high density area corresponds to the interface region, where most of the intermediate Si suboxide components (Si^{1+}, Si^{2+}, Si^{3+}) reside. Indeed, because the entering oxygen atoms are stopped by the silicon barrier energy, the interface is enriched in oxygen, which is translated into the mass distribution by two silica regions. Due to the relatively high energy, the silica surface contains many small craters (e.g., see atomic 1 eV in Figure 7). Therefore, the mass density of the surface silica (region IV) is lower than that of the silica bulk (region III). In Table 1, the thickness of the various regions, that is, interface, bulk silica, and surface silica, as estimated from the mass and partial charge distributions (cf. Figure 8) is presented for both the atomic and molecular impacts, at the three different impacting energies investigated. It can be seen from the table that the thickness is a nearly a linear function of the kinetic energy of the impinging oxygen species. The thickness of the layer obtained by atomic oxygen is almost twice the value obtained for molecular oxygen. Indeed, these observations suggest that the thickness of the layer can be controlled by the choice of the impinging species and the impinging energy.

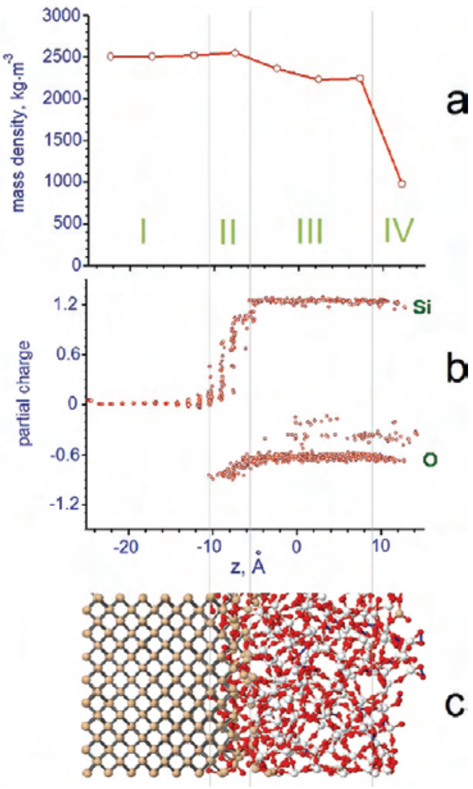

Figure 8. (a) Calculated mass density distribution and (b) partial charge distribution of the pure Si and oxygenated Si layer. (c) Schematic representation of the oxygenated silicon structure. The different regions are clearly indicated in (b): (I) pure Si; (II) interface; (III) SiO_2 bulk; and (IV) SiO_2 surface.

Table 1. Final Thickness of the Oxygenated Silicon, Split up into Interface, Bulk Silica, and Surface Silica Regions, for Both Atomic and Molecular Impacts at the Three Different Energies Investigated, as Estimated from the Mass and Partial Charge Distributions[a]

		thickness of oxygenated silicon, Å				
			silica (SiO_2)			
incident oxygen species	incident energy, eV	interface	bulk	surface	total	total
atom	1.0	5.5	9.9	5.3	15.2	20.7
	3.0	5.6	11.9	5.0	16.9	22.5
	5.0	5.8	13.5	5.2	18.7	24.5
molecule	1.0	4.8	2.9	2.3	5.2	10.0
	3.0	5.2	4.9	1.4	6.3	11.5
	5.0	5.6	7.0	2.1	9.1	14.7

[a] See Figure 8.

3.2.3. Analysis by Means of the Radial Distribution Function (RDF). Figure 9a shows the total radial distribution functions (RDF) of the obtained bulk silica structures for the atomic and molecular oxidation with kinetic energies of 1, 3, and 5 eV. The Si−O, O−O, and Si−Si bonds (β, γ, and δ peaks, respectively, in figure 9a), are found to be 1.61, 2.51, and 3.15 Å, respectively, at all cases investigated, that is, both atomic and molecular impacts, at the three different impact energies. These values agree with both experimental values and other MD calculations[15,32,50] and indicate that the obtained structure is amorphous.

Some unexpected O−O nonbonded neighbors (γ' peak) are found with distance 2.25 Å, close to the γ peak. We believe this

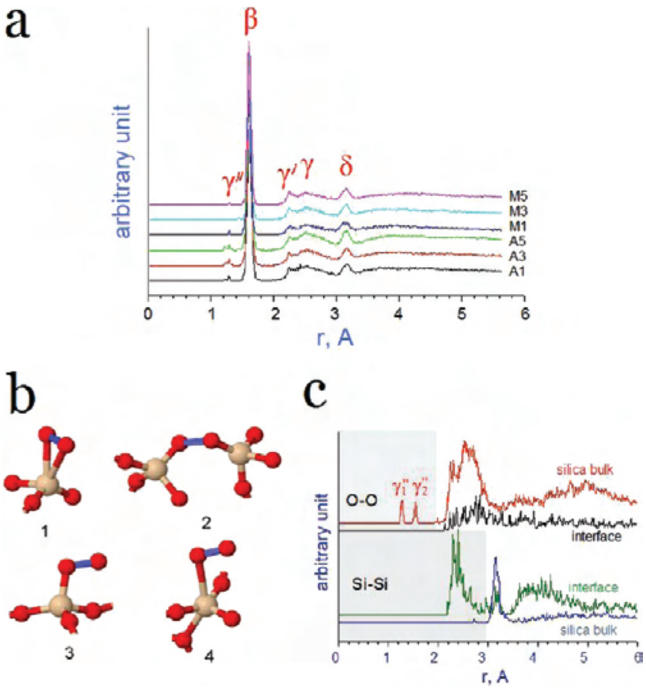

Figure 9. (a) Total radial distribution functions (RDFs) of the SiO_2 bulk silica structures, for the atomic and molecular impacts at the three different impact energies investigated, (b) some oxygen peroxyl bridge bonds in silica, and (c) RDFs of O−O and Si−Si in both bulk silica and interface.

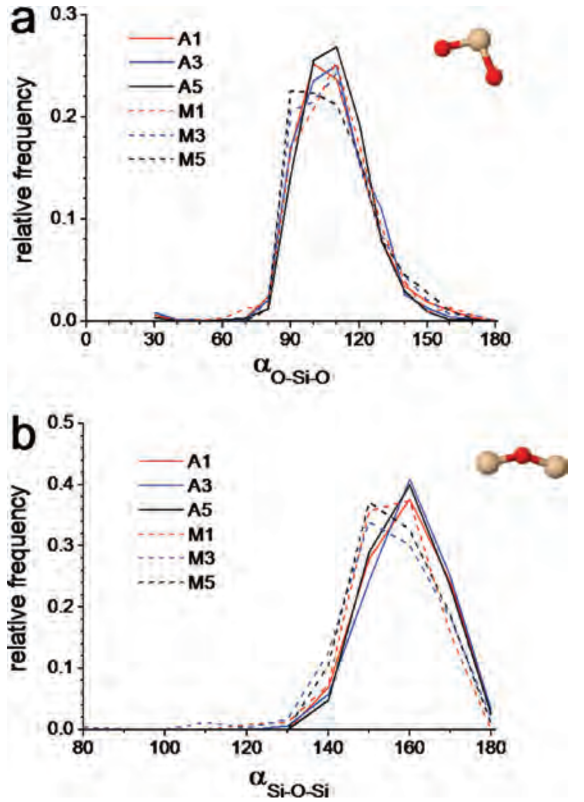

Figure 10. Distribution of (a) the O−Si−O and (b) the Si−O−Si angles in the SiO_2 bulk silica structures, for the atomic and molecular impacts at the three different impact energies investigated.

peak is caused by stresses near the interface. Also, the γ' peak depends on the silica thickness, that is, an increasing in the ultrathin silica thickness significantly decreases such O−O in tetrahedral silicon structure. Furthermore, a γ'' peak indicates that the silica film contains also O−O peroxyl bonds, both in the bulk as well as at the surface. In our structures, two types of peroxyl bonds are found (indicated as 1 and 2 in Figure 9b), which correspond to the γ_1'' and γ_2'' peaks in Figure 9c. The existence of peroxyl bridges and three-fold bond configurations in amorphous SiO_2 has already been suggested on the basis of some experimental and first-principles calculations.[17,48,51] Indeed, it was suggested that the peroxyl bridge configuration is energetically more stable than the three-fold oxygen bond (O^{3-}) configuration, in which oxygen is linked to three silicon atoms. Our results also show that such peroxyl bonds occur more in the silica induced by atomic oxidation than by molecular oxidation, although their contributions to the total RDF is small. Indeed, most peroxyl oxygen atoms do not originate from one oxygen molecule but rather appear in the silica bulk after impact. The appearance of the peroxyl bridge bonds reduces the silica mass density. This explains the slightly lower mass density of the obtained silica bulk during atomic oxidation compared to the silica obtained by molecular oxidation. Indeed, such peroxyl bonds were almost absent in the molecular oxidation case.

Moreover, due to diffusion, the peroxyl bridges in silica may temporarily link to silicon atoms, increasing the number of metastable overcoordinated silicon atoms as indicated by 3 and 4 in Figure 9b. Some first-principles calculations[12,51] predicted that oxygen molecules or peroxyl bonds can also diffuse without linking to Si and that the diffusivity depends on the ring size, which appears during silica formation. Furthermore, it is shown in Figure 9c that O−O bonds with bond distances less than 2.0 Å are not found in the interface. Indeed, the peroxyl oxygen atoms only exist in the silica bulk, and they break when they enter the interface region. Also Si−Si bonds (oxygen vacancies)[48] are found in both the interface and silica regions, albeit in very low concentration. Our results are in agreement with both experimental and first-principle calculations, indicating that the existence of the oxygen vacancy and diffusion of the peroxyl bridge bonds could play a role in the oxidation of the interface region during the formation of ultrathin silica films.

3.2.4. Analysis by Means of Angle Distribution. In agreement with the assessment established based on the RDF data, the angle distribution in the bulk silica structures indicates an amorphous structure. Figure 10a presents O−Si−O angle distributions in the silica region. In this distribution, most angles are distributed around 110° in the atomic oxidation case, and this value corresponds to the tetrahedral silicon structure (this angle in α-quartz is the tetrahedral angle of 109°). However, the peak slightly shifts to 90° in the molecular case due to either stress near the interface or oxygen peroxyl bonds. Amorphous silica structure is characterized by the Si−O−Si angles. For comparison, the Si−O−Si angle in α-quartz is 144°. In the case of amorphous silica, slightly differing mean values of the Si−O−Si angle distribution were reported. Mozzi and Warren[50] reported on the vitreous (amorphous) silica structure, which is obtained by oxidation of thermal O_2, citing Si−O−Si angles widely distributed in the range 120−180°, while a peak in this distribution was found at 144°. Furthermore, Watanabe et al.[52] investigated thermal growth by large-scale molecular dynamics, and they concluded that the Si−O−Si bond angle in ultrathin SiO_2 film is reduced from 144° toward a narrower angle in the range 130−140°. Moreover, Mauri et al.[53] found a slightly higher mean value (i.e., 151° ± 11°) and a relatively narrow distribution (120−170°), in the Si−O−Si angular distribution of vitreous silica. However, in our case, corresponding to hyperthermal oxidation, two peaks in the Si−O−Si angle distribution were found around 145° and 160°, as illustrated in Figure 10b. The first peak is in good agreement with results[50] of thermal O_2 oxidation. However, the second peak of the Si−O−Si distribution is slightly shifted to higher values, especially in the atomic oxidation case. Indeed, peroxyl oxygen bonds significantly affect the structures. As mentioned above, a relatively high number of oxygen peroxyl bridge bonds are found to be formed during the atomic oxidation process. Furthermore, about 3% the Si−O−Si angles near 110° are found, which indicates that some oxygen atoms have three silicon neighbors. Indeed, the contribution of oxygen peroxyl bridge (O−O) bonds, three-fold coordinated oxygen (O^{3-}) atoms and five-fold coordinated silicon (Si^{5+}) atoms in the silica, widens the range of both the O−Si−O and Si−O−Si angle distributions, respectively. Although some intrinsic defects are found in the silica, the overall spread in the angle distribution confirms the amorphous character of the SiO_2 structure.

4. SUMMARY AND CONCLUSIONS

The growth behavior of ultrathin silica during the hyperthermal oxidation process (with kinetic energies in the range 1−5 eV) at room temperature is investigated by reactive molecular dynamics.

Our results show that hyperthermal oxidation consists of an initial fast and a subsequent slow oxidation stage. In the initial oxidation stage, incident oxygen species can penetrate deeper than the Si topmost surface and directly oxidize Si subsurface layers, in contrast to thermal oxidation. The oxygen atoms cannot move deeper into the bulk due to the associated activation energy barrier. The limit depth of the penetrating O species is deeper in the atomic oxygen case compared to the molecular one.

We also analyzed the oxygenated silicon structure by dividing it into three regions, that is, silica bulk, a transition layer, and the surface. The oxygenated silicon is energetically more stable than pure silicon. In all cases, the thickness of the transition layer is about 5 Å, and surface roughness of the interface is low. A linear growth of the silica thickness in the earlier oxidation stage was observed. The silica thickness of the layers grown by molecular oxygen with an energy of 3 eV and atomic oxygen with 5 eV become about 6 Å and 19 Å, respectively, in agreement with experimental data. Therefore, we conclude that the silica thickness can be controlled by controlling the initial kinetic energy of incident oxygen at room temperature.

The radial distribution function (RDF) indicates that the silica bulk contains some intrinsic defects (i.e., incorrect coordination of Si or O atoms, oxygen vacancies) and oxygen peroxyl linkages, both in the bulk as well as at the surface. Diffusion of peroxyl oxygen bridges could play a role in the oxidation during the formation of ultrathin silica films. The overall spread of the angle distribution confirms the amorphous character of the SiO_2 structure.

We conclude that the control of the ultrathin SiO_2 thickness is possible by a hyperthermal oxidation of silicon surfaces at room temperature. This control over the obtained silica layer thickness is of great importance for technological applications.

■ ASSOCIATED CONTENT

Ⓢ Supporting Information. Full set of ReaxFF parameters used in this study. This material is available free of charge via the Internet at http://pubs.acs.org.

■ AUTHOR INFORMATION

Corresponding Author

*E-mail: umedjon.khalilov@ua.ac.be.

■ ACKNOWLEDGMENT

U. Khalilov acknowledges IMEC for financial support. E. Neyts acknowledges the FWO-Flanders (Fund for Scientific Research-Flanders) for financial support. A. van Duin acknowledges funding from the Air Force Office of Scientific Research (AFOSR) under grant no. FA9550-10-1-0563. The authors also gratefully acknowledge financial support from the Prime Minister's Office through IAP VI. This work was carried out using the Turing HPC infrastructure at the CalcUA core facility of the Universiteit Antwerpen (UA), a division of the Flemish Supercomputer Center VSC, funded by the Hercules Foundation, the Flemish Government (department EWI) and the UA.

■ REFERENCES

(1) International Technology Roadmap for Semiconductors 2010 edition (http://www.public.itrs.net/).

(2) Pasquarello, A.; Stoneham, A. M. *J. Phys.: Condens. Matter* **2005**, *17*, V1–V5.

(3) Teraoka, Y.; Yoshigoe, A. *Surf. Sci.* **2002**, *507−510*, 797–802.

(4) Yoshigoe, A.; Teraoka, Y. *Surf. Sci.* **2003**, *532−535*, 690–697.

(5) Enta, Y.; Mun, B. S.; Rossi, M.; Ross, P. N.; Hussain, Z., Jr.; Fadley, C. S.; Lee, K.; Kim, S. *Appl. Phys. Lett.* **2008**, *92*, 012110.

(6) Green, M. A. *Nanotechnology* **2000**, *11*, 401–405.

(7) Stoneham, A. M. *J. Non-Cryst. Solids* **2002**, *303*, 114–122.

(8) Bongiorno, A. *Simulation of atomistic processes during silicon oxidation*, PhD thesis, Lausanne, EPFL, 2003; and references therein.

(9) Deal, B. E.; Grove, A. S. *J. Appl. Phys.* **1965**, *36*, 3770–3778.

(10) Gusev, E. P.; Lu, H. C.; Gustafsson, T.; Garfunkel, R. *Appl. Surf. Sci.* **1995**, *104*, 329–334.

(11) Gusev, E. P.; Lu, H. C.; Gustafsson, T.; Garfunkel, R. *Phys. Rev. B* **1995**, 52and references therein.

(12) Bongiorno, A.; Pasquarello, A. *J. Mater. Sci.* **2005**, *40*, 3047–3050.

(13) Massoud, H. Z.; Plummer, J. D.; Irene, E. A. *J. Electrochem. Soc.* **1985**, *132*, 1745.

(14) Irene, E. *Solid-State Electron.* **2001**, *45*, 1207–1217.

(15) Pasquarello, A.; Hybertsen, M.; Car, R. *Appl. Surf. Sci.* **1996**, *104/105*, 317–322.

(16) Bongiorno, A.; Pasquarello, A. *Mater. Sci. Eng., B* **2002**, *96*, 102–106.

(17) Ng, K.-O.; Vanderbilt, D. *Phys. Rev. B* **1999**, *59*, 10132–10137 and references therein.

(18) Giustino, F.; Bongiorno, A.; Pasquarello, A. *J. Phys.: Condens. Matter* **2005**, *17*, S2065–S2074.

(19) Kageshima, H.; Shiraishi, K. *Phys. Rev. Lett.* **1998**, *81*, 5936–5939.

(20) Tzvetkov, T.; Qin, X.; Jacobs, D. C. *Phys. Rev. B* **2003**, *67*, 075418.

(21) Tagawa, M.; Sogo, C.; Yokota, K.; Yoshigoe, A.; Teraoka, Y.; Shimura, T. *Appl. Phys. Lett.* **2006**, *88*, 133512and references therein.

(22) Kisa, M.; Minton, T. K.; Yang, J. C. *J. Appl. Phys.* **2005**, *97*, 23520.

(23) Cerofolini, G. F.; Meda, L. *J. Non-Cryst. Solids* **1997**, *216*, 140–147.

(24) Cerofolini, G. F.; Mascolo, D.; Vlad, M. O. *J. Appl. Phys.* **2006**, *100*, 054308.

(25) van Duin, A. C. T.; Dasgupta, S.; Lorant, F.; Goddart, W. A., III *J. Phys. Chem. A* **2001**, *105*, 9396–9409.

(26) Abell, G. C. *Phys. Rev. B* **1985**, *31*, 6184–6196.

(27) Mortier, W. J.; Ghosh, S. K.; Shankar, S. *J. Am. Chem. Soc.* **1986**, *108*, 4315–4320.

(28) van Duin, A. C. T.; Baas, J. M. A.; van de Graaf, B. *J. Chem. Soc., Faraday Trans.* **1994**, *90*, 2881–2895.

(29) van Duin, A. C. T.; Strachan, A.; Stewman, S.; Zhang, Q.; Xu, X.; Goddard, W. A., III *J. Phys. Chem. A* **2003**, *107*, 3803–3811.

(30) Buehler, M. J.; van Duin, A. C. T.; Goddard, W. A. *Phys. Rev. Lett.* **2006**, *96*, 095505.

(31) Ning, N.; Calvo, F.; van Duin, A. C. T.; Wales, D. J.; Vach, H. *J. Phys. Chem. C* **2009**, *113*, 518–523.

(32) Fogarty, J. C.; Aktulga, H. M.; Grama, A. Y.; van Duin, A. C. T.; Pandit, S. *J. Chem. Phys.* **2010**, *132*, 174704and references therein.

(33) Quenneville, J.; Taylor, R. S.; van Duin, A. C. T. *J. Phys. Chem. C* **2010**, *114*, 18894–18902.

(34) Valentini, P.; Schwartzentruber, T. E.; Cozmuta, I. *J. Chem. Phys.* **2010**, *133*, 084703.

(35) Mueller, J. E.; van Duin, A. C. T.; Goddard, W. A., III *J. Phys. Chem. C* **2010**, *114*, 5675–5685and references therein.

(36) Berendsen, H. J. C.; Postma, J. P. M; van Gunsteren, W. F.; DiNola, A.; Haak, J. R. *J. Chem. Phys.* **1984**, *81* (8), 3684–3690.

(37) Tagawa, M.; Yokota, K.; Tsumamoto, S.; Sogo, C.; Yoshigoe, A.; Teraoka, Y. *Appl. Phys. Lett.* **2007**, *91*, 033504.

(38) Murad, E. *J. Spacecr. Rockets* **1996**, *33*, 131.

(39) Tagawa, M.; Yokota, K.; Ohmae, N.; Kinoshita, H.; Umeno, M. *Jpn. J. Appl. Phys., Part 1* **2001**, *40*, 6152.

(40) Ganster, P.; Treglia, G.; Saul, A. *Phys. Rev. B* **2010**, *81*, 045315.

(41) Kato, K.; Uda, T.; Terakura, K. *Phys. Rev. Lett.* **1998**, *80*, 2000.

(42) Watanabe, H.; Kato, K.; Uda, T.; Fujita, K.; Ichikawa, M.; Kawamura, T.; Terakura, K. *Phys. Rev. Lett.* **1998**, *80*, 345–348.

(43) Neyts, E.; Khalilov, U.; Pourtois, G.; van Duin, A. C. T. *J. Phys. Chem. C* **2011**, *115* (11), 4818–4823.

(44) Choi, C. H.; Liu, D.; Evans, J. W.; Gordon, M. S. *J. Am. Chem. Soc.* **2002**, *124*, 8730–8740.

(45) Oh, J. H.; Nakamura, K.; Ono, K.; Oshima, M.; Hirashita, N.; Niwa, M.; Toriumi, A.; Kakizaki, A. *J. Electron Spectrosc. and Relat. Phenom.* **2001**, *114—116*, 395–399.

(46) Tu, Y.; Tersoff, J. *Phys. Rev. Lett.* **2000**, *84*, 4393.

(47) van Ginhoven, R. M.; Hjalmarson, H. P. *NIM B.* **2007**, *255*, 183–187.

(48) Stoneham, A. M.; Szymanski, M. A.; Shluger, A. L. *Phys. Rev. B* **2001**, *63*, 221304–07and references therein.

(49) Newton, M. D.; Gibbs, G. V. *Phys. Chem. Miner.* **1980**, *6*, 221.

(50) Mozzi, R. L.; Warren, B. E. *J. Appl. Crystallogr.* **1969**, *2*, 164–172.

(51) Bakos, T.; Rashkeev, S. N.; Pantelides, S. T. *Phys. Rev. Lett.* **2002**, *88* (5), 055508.

(52) Watanabe, T.; Tatsumura, K.; Ohdomari, I. *Appl. Surf. Sci.* **2004**, *237*, 125–133.

(53) Mauri, F.; Pasquarello, A.; Pfrommer, B. G.; Yoon, Y.-G.; Louie, S. G. *Phys. Rev. B* **2000**, *62*, 4786–4789.